Materials Science & Engineering A 764 (2019) 138168

Contents lists available at ScienceDirect

Materials Science & Engineering A

journal homepage: www.elsevier.com/locate/msea

The effect of strain path changes on texture evolution and deformation behavior of Ti6Al4V subjected to accumulative angular drawing

J. Kawałko[a,*], K. Muszka[b], P. Graca[b], M. Kwiecień[b], M. Szymula[b], M. Marciszko[a], P. Bała[a,b], Ł. Madej[b], I.J. Beyerlein[c]

[a] AGH University of Science and Technology, Academic Centre for Materials and Nanotechnology, Al. A. Mickiewicza 30, 30-059, Krakow, Poland
[b] AGH University of Science and Technology, Faculty of Metals Engineering and Industrial Computer Science, Al. A. Mickiewicza 30, 30-059, Krakow, Poland
[c] Department of Mechanical Engineering, Materials Department, University of California, Santa Barbara, Santa Barbara, CA, 93106-5070, United States

ARTICLE INFO

Keywords:
Accumulative angular drawing
Titanium alpha beta alloy
Microstructure
Texture analysis
Slip systems
Hardness
Tensile tests

ABSTRACT

The Ti–6Al–4V alloy wires were plastically deformed using the accumulative angular drawing (AAD) process at room temperature with a maximal logarithmic strain $\varepsilon \sim 0.51$. Microstructure and microtexture evolution and inhomogeneity of the Ti alloy wires were investigated quantitatively using the electron backscattered diffraction technique within the scanning electron microscope and compared to wires after conventional linear drawing. Moderate grain refinement was observed after deformation. The kernel average misorientation parameter increased significantly, pointing to evolution of subgrain structure. The yield stress and ultimate tensile strength increased after the AAD and linear drawing and decrease in hardness was observed after the first pass of the AAD and linear drawing process. However, the AAD introduced inhomogeneity in hardness values at the sample cross section. Hardness variation correlates with a local texture asymmetry parameter, while no correlation between hardness and grain size was observed. A Schmid factor analysis indicated that the AAD is inhomogeneously introducing grain orientations that are favorable for prismatic and pyramidal dislocation slip, having a positive effect on the plasticity of Ti–6Al–4V alloy wire during drawing.

1. Introduction

Titanium alloys are widely used in aerospace, chemical, and medical industries due to their high specific strength and excellent corrosion resistance [1,2]. One of the most commonly used titanium alloys in industry, the “workhorse” alloy, is Ti–6Al–4V, which is a two phase α+β alloy, consisting of a hexagonal close packed α phase and a body centered cubic β phase [3]. It is largely used to make various fasteners, such as bolts and rivets, for the aerospace industry. Producing parts in this shape involves wire drawing and subsequent forging. One of the most important steps in the Ti6Al4V production process is the former drawing step. Unfortunately, due to a low number of easily activated slip systems in the α-phase, plastic deformation at room temperature is limited. In order to achieve wires of sufficiently fine diameters for forging, the drawing process of Ti6Al4V is performed at elevated temperature, which results in a number of problems such as the unwanted grain growth, the potential development of hard and brittle alpha case, and an increased rate of tool wear.

The limited plasticity during wire drawing is connected to the strong plastic anisotropy of the hcp α Ti phase. The dislocation slip underlying plasticity can occur either in the *a* direction on the (0002) basal and $\{10\bar{1}0\}$ prismatic planes, or in the $c + a$ direction on the $\{10\bar{1}1\}$ 1st order, and $\{11\bar{2}2\}$ 2nd order pyramidal planes [4]. Between the two types of < a > slip, the $\{10\bar{1}0\}$ prismatic slip is the preferred one for the α Ti phase. At room temperature, the critical resolved shear stresses (CRSS) for the $c + a$ slip is approximately twice as high as that for the prismatic slip [1]. Generally in the α Ti and its alloys, the hard $c + a$ slip can be replaced by deformation twinning, with the main twinning modes being $\{10\bar{1}2\}$, $\{11\bar{2}1\}$, and $\{11\bar{2}2\}$ [1]. Twinning accommodates *c* axis deformation and, therefore, can compete with the pyramidal $c + a$ slip, particularly when the crystal is poorly oriented for deformation in the < a > direction. However, in the Ti6Al4V the presence of aluminum effectively suppresses twinning and thus the $c + a$ slip becomes an important mechanism controlling the plasticity of the Ti6Al4V alloy [4]. Strong preference for the $\{10\bar{1}0\}$ prismatic slip over $c + a$ slip promotes localization of slip bands on the $\{10\bar{1}0\}$ prismatic planes, in those grains that are initially suitably oriented for the prismatic slip and those that reorient with deformation to orientations that are suitable for the prismatic slip.

A related factor contributing to a limited ductility is texture

* Corresponding author.
E-mail address: kubaka@agh.edu.pl (J. Kawałko).

https://doi.org/10.1016/j.msea.2019.138168
Received 23 March 2019; Received in revised form 12 July 2019; Accepted 15 July 2019
Available online 16 July 2019
0921-5093/

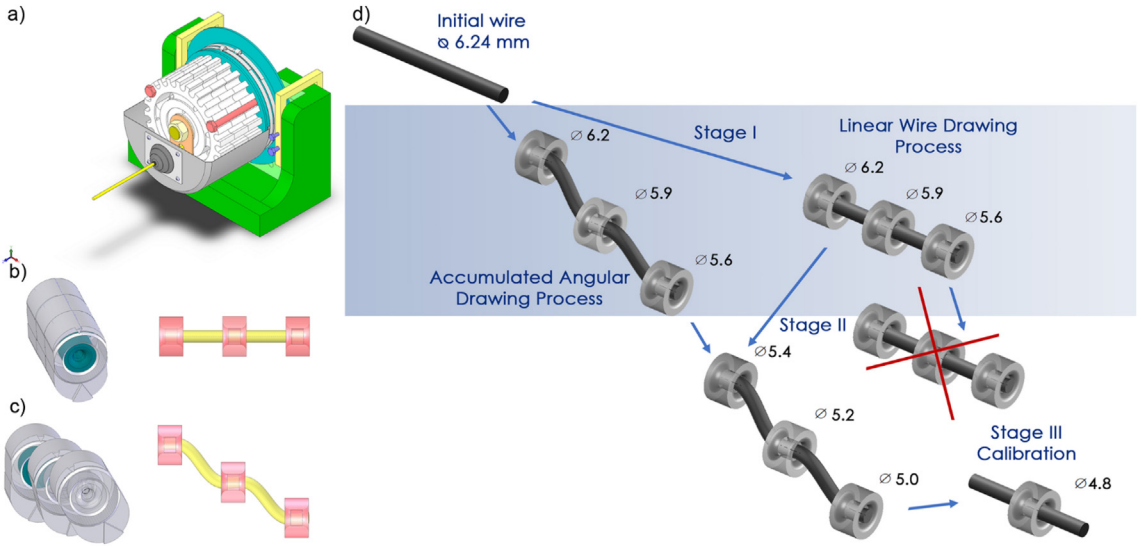

Fig. 1. Angular Accumulative Drawing method: a) the AAD tool; b) the linear drawing setup; c) the stepped drawing setup; d) applied deformation schedule.

development. During the drawing process, the Ti6Al4V wire becomes strongly textured with a typical fiber texture [5], wherein the [0001] directions are perpendicular to the drawing direction, and $\{10\bar{1}0\}$ poles are highly oriented parallel to the drawing direction. In this orientation, most grains become favorably oriented for the prismatic slip. Consequently as strain accumulates with repeated drawing steps, slip localizes on the prismatic slip planes, the crystals rapidly work harden, failure ensues, and the plastic regime ends.

The accumulative angular drawing (AAD) is a recently developed technique that is able to circumvent the aforementioned issues and produce wires with enhanced microstructure and mechanical properties [6,7]. Fig. 1 shows the AAD equipment set up. The AAD allows for the controlled introduction of complex strain paths, such as bending, burnishing, shearing and torsion, into the drawing process. Such a composite of deformation modes generates complex internal stress and strain states, which can increase the number of active slip systems and the shear provided by them, distributing slip in the individual crystals. Mechanically diffusing slip can thwart the tendency for the material to localized slip, even in materials such as the Ti6Al4V, which intrinsically prefer to slip using predominantly their easiest slip system. Accordingly, complex strain paths can potentially extend the plastic regime. Severe plastic deformation techniques with changing strain paths, such as ECAP [8,9] or KoBo [10,11], have enabled titanium and titanium alloys to achieve large strains and produced materials with extended plasticity. These methods, however, still require specialized equipment and elevated processing temperatures. The AAD setup, on the other hand, uses existing wire drawing facilities.

In this work, application of the complex strain path and strain path changes via the AAD (Fig. 1d) is used to successfully deform the Ti6Al4V wire to large strains at room temperature. The microstructure of the resulting wires is then investigated using the electron backscattered diffraction (EBSD) in the scanning electron microscope (SEM) to evaluate the influence of local heterogeneities, initially identified numerically (Fig. 2), on the material response.

2. Experimental methods

The drawing process was realized with the AAD tool that is presented in Fig. 1a. It consists of 3 resistive plates in which the drawing dies are placed very close to each other. Position of the consecutive drawing dies can be changed both in the circumferential and radial direction. This way, different strain path can be applied. In the current work, two positionings of the dies were used: (1) stepped die positioning (Fig. 1c), where the consecutive drawing dies were twisted with respect to each other by an angle of 7° while their radial positions were constant; and (2) linear positioning (Fig. 1b), where the drawing dies were mounted at the same positions in the resistive plates, so the was no change of strain path, and thus, the process was realized in a similar way to traditional wire drawing, where only area reduction is used as the deformation mechanism.

In the current studies, three stages of drawing were realized (see Fig. 1d). In the first stage, the initial wire rod with the diameter of 6.24 mm was drawn down to the diameter of 5.6 mm with three drawing dies. For comparison purposes this process was realized with stepped dies positioning (marked as AAD) and with linear dies positioning (marked as LIN). During the 2nd stage, the wire was further deformed – without any annealing – down to the diameter of 5.0 mm. This time, however, the deformation process was only possible with the complex strain path (AAD) – the linear drawing was not successful (the wire was breaking). It is interesting to note, however, that the application of the complex strain path (AAD) to the wire that was previously drawn in the linear manner, was successful. Finally, the 3rd drawing stage was applied – the calibration stage. This stage was realized using only one drawing die and the final diameter of the wire was 4.8 mm.

The initial material was Ti6Al4V wire rod provided in the as-hot rolled conditions with its diameter of 6.24 mm. Before the drawing process, the surface of the wire was treated with a NaCl dissolved in hot water. This operation ensures the proper application and adherence of the lubricant (MoS_2) during the AAD process. Before the drawing, the wire's surface was marked with 3 scratches (along the surface of the wire) in order to track the position of the wires during the drawing. The wire drawing process was realized with very small speed (2 mm/min) so the temperature raise due to plastic deformation was negligible. After every stage of the drawing, from each wire, two samples for tensile tests were cut. The quasi-static tensile tests were performed using the Zwick 200 kN tensile frame to assess both mechanical properties and ductility.

Presented in Fig. 2 FEM modelling results confirm that during the AAD equivalent plastic strain distribution, both along the length and at the cross-section of the drawn wire is much more inhomogeneous, compared to the typical, linear wire drawing process. This suggests that additional deformation mechanisms, that are characteristic for the AAD (shearing, bending, burnishing), may have beneficial effect on room temperature deformation of Ti6Al4V activating more slip systems.

The complex strain paths and severe strains are expected to lead to substantial texture development. Here the effect of applied strain path

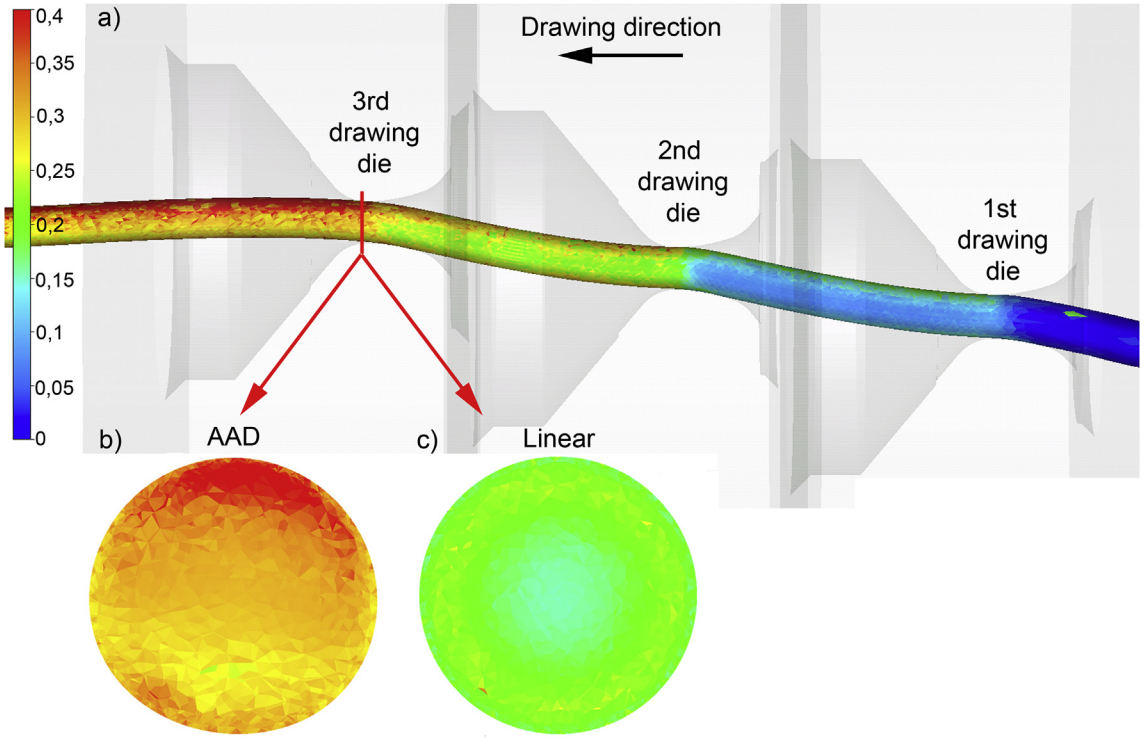

Fig. 2. Inhomogeneity of equivalent plastic strain along a) the surface of the AAD drawn wire and comparison of equivalent plastic strain distribution at the cross-section of the wire drawn in the b) AAD and c) linear manner.

history on texture development, grain shape, grain size, and sub-crystalline misorientation in the Ti6Al4V wire samples after the drawing process were investigated by means of the EBSD mapping in the high-resolution FEI Versa 3D SEM. To estimate dislocation densities in deformed samples the XRD measurements were made using PANalytical Empyrean X-ray diffractometer (Cu Kα radiation) with the step size 0.01° at the room temperature. The TEM investigations were performed using FEI Tecnai TF-20 X-TWIN microscope. Samples for microstructure characterization were prepared by sectioning with a SiC cut-off wheel, followed by mechanical grinding with SiC papers up to a grit 4000. Finely ground samples were subsequently polished using a colloidal silica suspension with the addition of hydrogen peroxide. Polishing times of up to 30 min were used to achieve flat, deformation-free surfaces suitable for investigation with the EBSD technique and the XRD measurements. Samples for the TEM observations were prepared by the twin-jet electropolishing using Struers A3 electrolyte at 35 V and −30 °C.

Microstructural studies were performed on samples after different stages in the AAD process. For comparison, we also evaluated samples deformed to nominally the same drawing strain as the AAD but by a conventional, linear (LIN) wire drawing process. In what follows, samples are designated by the starting wire diameter (INIT 6.2), process used (AAD or LIN) and the final wire diameter in mm. EBSD maps were collected from 60 µm × 60 µm areas of the samples with a step size of 100 nm. In the case of the INIT 6.2, AAD 5.6, and AAD 4.8 samples, the investigations were carried out at transverse (trans), and longitudinal (long) cross sections of the drawn wires, i.e. from surfaces perpendicular and parallel to the drawing direction. In addition, Vickers hardness mapping of the cross-section surface combined with the EBSD analysis was performed for the initial 6.2 samples and after the first strain step via the AAD (AAD 5.6) and the linear drawing (LIN 5.6). A 2.94 N force was used for each indent.

In anticipation of processing induced heterogeneities in the microstructure from the surface to center, EBSD scans and Vickers hardness tests were conducted at different areas of the wire cross-section. Fig. 3

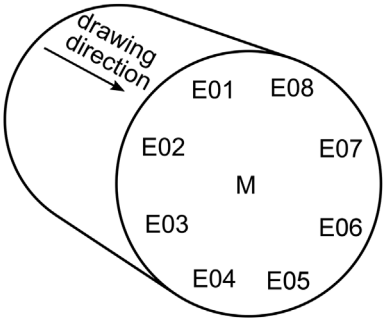

Fig. 3. Schematic presentation of the EBSD and Vickers hardness analysis placements. Analyses were performed in eight areas close to a surface of the wire (E01-E08), and in the middle of the wire (M).

shows the location of these measurements in the case of the AAD 5.6 wire. For the LIN 5.6 and INIT 6.2 samples, the measurement areas were selected arbitrarily, as the samples were not subjected to axially asymmetrical process; however, the same counter-clockwise convention of the measurement area numbering presented in Fig. 3 is used. Vickers hardness measurements were performed in these nine areas. In each area a total of nine Vickers indents were performed in 3 × 3 matrices, with a 200 µm distance between indents, and at least 200 µm between indents and the surface of wire. For each area, an average hardness value and standard error of the mean were calculated. For the AAD 5.6 sample, EBSD maps were collected in the same nine regions as the hardness measurement areas and in the same nine selected areas for the LIN 5.6 sample, and three areas for the INIT 6.2 sample.

From each the EBSD scan, grain size distributions and kernel average misorientation (KAM) were obtained. A grain in this case is defined as a group of minimum five points with a neighbor to neighbor misorientation angle below 15°. The size of a grain is measured as the diameter of the equivalent circle approximating each grain. The mean grain diameter was calculated as area weighted averages. KAM values

were calculated for one neighbor kernels with a maximum misorientation of 15°, and then, the average KAM value was calculated for each measured EBSD map.

Local microtexture analysis was performed using all collected EBSD maps. Pole figures (PF) for the main crystallographic hcp directions: (0002), $(10\bar{1}0)$ and $(11\bar{2}0)$, were recalculated from orientation distribution functions (ODF) using Mtex software [12]. Before additional orientation analysis, the ODF from each EBSD map was subjected to a centering procedure in order to eliminate potential differences in orientations between samples due to imperfect sample sectioning. After the centering procedure, a pole figure asymmetry parameter was calculated based on the difference (error value) between the measured PF, and the same PF rotated by a specified angle around the z (normal) direction. For each PF analyzed, the error value was calculated for each original/rotated PF pair with rotation angle values from 5° to 180° with 5° step. Calculated error values were then averaged over all rotation angles resulting in an average error–asymmetry parameter for each PF.

Additional orientation analysis based of calculation of Schmid factors for the prismatic and pyramidal $c + a$ slip systems was also performed using the Mtex software. The distributions of Schmid factors for each EBSD map were calculated based on the orientation data corrected using the rotations obtained from the ODF centering procedure.

3. Results

3.1. The microstructure evolution during accumulative angular drawing

Fig. 4 shows the initial microstructure of the Ti6Al4V wire using the EBSD maps. Statistical analysis indicates that the initial microstructure consists of alpha-phase grains, varying widely in grain sizes from 0.5 to 6 μm and containing well developed subgrain structure, as well as a small number of fine beta-phase grains, located predominately at the alpha grain triple junctions. Grains observed in the longitudinal cross section (Fig. 4b) are elongated in the direction parallel to the wire axis. In both cross sections, subgrain structures are observed inside the relatively larger grains in the form of low angle grain boundaries.

Local changes of grain orientations are visible, indicating presence of the geometrically necessary dislocations (GND). The GND content (density) can be associated with increased average KAM value [13] (1.32°) typical for materials after thermomechanical working, which in this case, is the hot rolled initial wire rod.

The data analysis indicate that the beta grains deform more heavily than the alpha grains. The quality of the EBSD data can be measured by the indexing rate, where a high number indicates data from which orientations can be accurately assessed. After the first stage of the deformation (AAD 5.6 sample, Fig. 4c and d), the indexing rate of the beta phase is drastically reduced and the beta grains are no longer observed in the IPF map, while the indexing rate of the alpha phase remains relatively high. This evolution suggests that beta grains deform heavily during the drawing process, resulting in high number of stored dislocations, which leads to severe blurring of electron backscattered diffraction patterns, and prohibits accurate indexing. As a consequence, the white areas appear in the IPF maps, representing microstructure with heavily deformed crystal lattice. The mean grain diameter decreases from 2.68 μm in the initial state (INIT 6.2) to 2.01 μm after first deformation stage (AAD 5.6) in the transverse cross section (Fig. 4g), and from 5.62 μm to 4.55 μm in the longitudinal cross section (Fig. 4h). Grain refinement during the first stage of deformation results in an increased fraction of grains with a diameter below 1.5 μm; however, the large grains are still present in the microstructure. The average KAM value increases further to 1.80°. Analysis of the KAM values in microstructure fractions containing different ranges of grain size (Fig. 5a) suggests that the accumulation rate of the GND is similar in fine grains, as well as in the relatively larger grains.

After the third stage of the AAD process (the AAD 4.8 sample, Fig. 4 e,f), only a slight additional microstructure refinement is observed at the transverse cross section (average grain size 2.02 μm), and at the longitudinal cross section, the average grain size is reduced to 4.06 μm. The average value of KAM increases slightly to 1.81°, suggesting that the GND density does not increase during the third AAD stage. Average KAM in large grain fraction is slightly decreased, compared to AAD 5.6, which could be interpreted as a result of dynamic recovery during the AAD process. The DRX (dynamic recrystallization) has been observed for Ti alloys after ECAP, where the KAM values and dislocation density increased after the 1st and 4th pass and then decreased after the 8th pass, what was attributed to dynamic recrystallization and recovery [14]. In the case of the AAD the continuous dynamic recrystallization (CDRX) is more likely mechanism governing the evolution of the microstructure due to much lower strain accumulated per single pass and low temperature of deformation. During the CDRX accumulation of

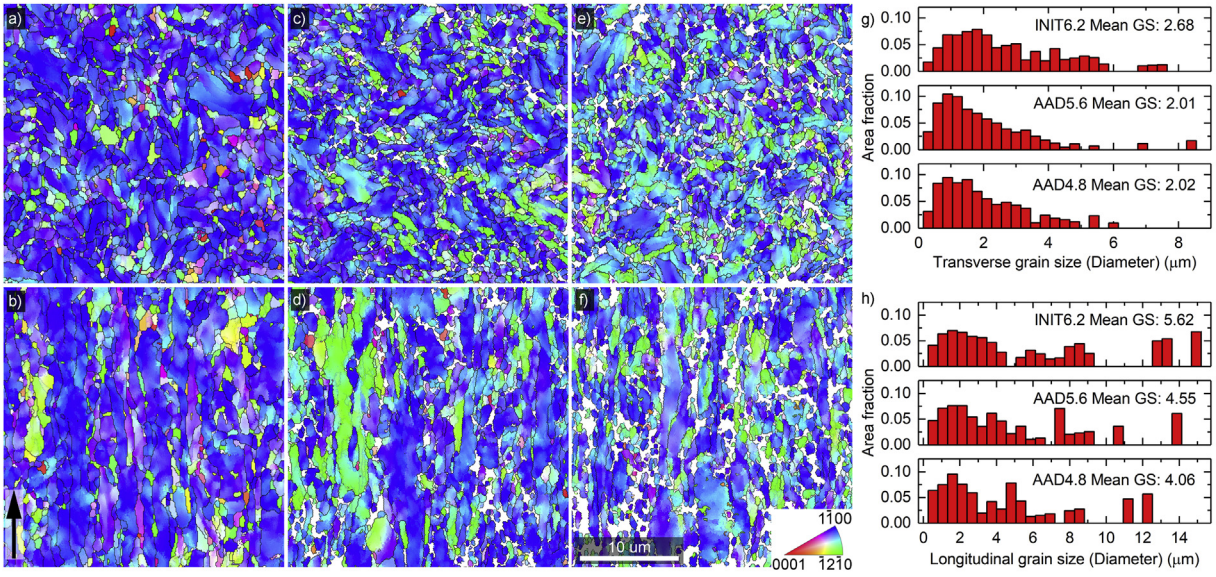

Fig. 4. Microstructure evolution during the AAD process. IPF crystal orientation maps (left), and grain size histograms (right) of transverse (upper row) and longitudinal cross sections (lower row) of Ti6Al4V samples: a,b) INIT 6.2; c,d) AAD 5.6; e,f) AAD 4.8. Black arrow in b) indicates the drawing direction. (For interpretation of the references to color in this figure legend, the reader is referred to the Web version of the article.). (For interpretation of the references to color in this figure legend, the reader is referred to the Web version of this article.)

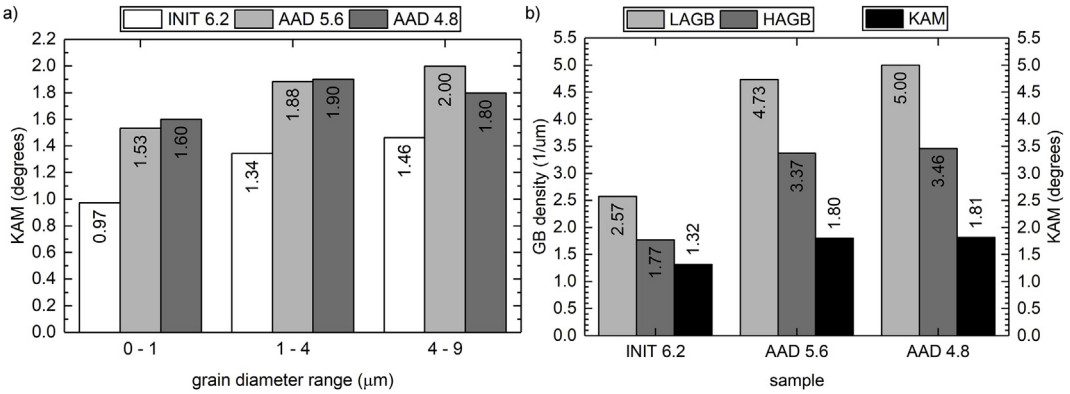

Fig. 5. a) KAM analysis in grain size fractions, b)grain boundary density in AAD samples.

dislocations the misorientation angle of the low angle grain boundaries (LAGB) gradually increases resulting in formation of the new high angle grain boundaries (HAGB) [15,16]. As seen in Fig. 5 b) both the LAGB and the HAGB density increases considerably after the first stage of the AAD. After the third AAD stage the LAGB increase is much lower suggesting that the LAGB to the HAGB transformation rate due to dislocation accumulation increased relatively to the rate of formation of the new LAGB. On the other hand, a visible increase in the number of white areas in the IPF maps, representing incorrect indexing of electron diffraction pattern in heavily deformed areas, suggests that deformation locally accumulates in regions adjacent to the boundaries of large grains and in the fine-grained regions of the microstructure, which may result in underestimation of the HAGB density as well as KAM values.

From the EBSD analysis, we find that the drawing process introduces additional crystallographic orientations into the microstructure. Orientations can be visualized in the IPF maps by changes of dominating colors between different stages of the deformation and also in the PFs presented in Fig. 6. The initial sample (INIT 6.2) has a $\{10\bar{1}0\}$ fibre texture typical for hcp metals after axially symmetric deformation process, such as extrusion, rolling or straight drawing [5]. In this texture, the $10\bar{1}0$ directions are oriented parallel to the wire direction, and the {0001} poles become evenly distributed in the plane perpendicular to the wire direction.

When the additional non-axially symmetric deformation is applied to the material during the AAD process, the texture begins to gradually deviate from the initial one. The asymmetry parameter (average error value) of $(10\bar{1}0)$ pole figure increases from 0.078 in the INIT 6.2 sample to 0.172 in the AAD 5.6 and to 0.174 in the AAD 4.8 samples. The increase in PF asymmetry after the third stage of the AAD process is much lower than after first one. This was expected from the numerical investigation as the orientation of titanium wire with respect to the AAD die assembly is not kept constant between drawing stages; therefore, additional non-axial deformation can occur in different directions at different stages. This randomization of deformation direction results in broadening of PF peaks, and decreased PF peak intensity, but not necessarily in increased asymmetry.

The mean error values of $(11\bar{2}0)$ PF: 0.082, 0.167 and 0.189 follow similar trends as in the case of the $(10\bar{1}0)$ PF, while the mean error values for the (0002) PF remains at low and nearly constant value: 0.069, 0.062 and 0.057 respectively for INIT 6.2, AAD 5.6 and AAD 4.8 samples. These texture changes could have resulted from prismatic dislocation slip since it is the main deformation mechanism operating during drawing of the Ti6Al4V wire. However, this result requires further evaluation via the TEM or crystal plasticity modelling.

3.2. Mechanical properties

The macro mechanical behavior of the AAD-processed wires is summarized in Fig. 7 by logarithmic strain-true stress curves acquired during an uniform tensile test performed on wires after subsequent stages of deformation. Also, uniform elongation of the deformed wires is assessed here using the Consideré criterion. It can be seen that during the second stage of the AAD process, the wire is characterized by an increased strength and uniform elongation, whereas during the final pass (AAD 4.8) both values slightly drop again. Most importantly, however, it should be noticed, that application of the AAD process increases both strength and ductility, compared to the linear drawing (after the first drawing pass).

The average hardness values for all sample areas are plotted in Fig. 8a. The distribution of values for AAD 5.6 sample points to inhomogeneity of mechanical properties across the cross section. The overall standard deviation of mean values for this sample is equal to 8.3, compared to 4.2, and 2.5 in the case of LIN 5.6, and INIT 6.2 samples respectively. This suggests that the inhomogeneity does not occur in the initial sample, and much lower inhomogeneity is obtained after linear drawing (LIN 5.6). Moreover, the inhomogeneity in case of AAD 5.6 results mostly from decreased hardness values measured in areas grouped together at the wire surface in the measurement areas E01, E02, E03 and E08, while in the case of LIN 5.6 the only outliner is the measurement in the middle of wire (M).

Variation of the hardness values across the cross section of the AAD 5.6 sample is not entirely compatible with the observed grain size variation. According to the Hall – Petch relation, there is a straight relation between grain size and mechanical properties. This however is not observed for the entire range of measured hardness values. In the case of AAD 5.6 local correlation can be found (for instance for sample areas E01, E02 and E03), on the other hand hardness in areas E05 and E07 is increased in relation to E01-E03, but grain size is almost the same.

Similarly, in the case of distribution of average KAM values, high KAM is not associated with increased hardness, what would be expected in areas with higher density of accumulated dislocations. This analysis suggests that the microstructural features are not solely responsible for the variation of mechanical properties on the Ti6Al4V cross section after the AAD process, and therefore it is suspected that texture effects are influencing the measured properties.

3.3. Microtexture

Local microtexture was analyzed using $(10\bar{1}0)$ PF calculated from the EBSD data collected in 9 areas on the Ti6Al4V sample cross-sections. Calculated PF are presented in Fig. 9. Both types of deformed samples have certain degree of asymmetry introduced to the pole figures during the drawing process. Common feature in all figures is a slight ellipticity of the central peak corresponding to $\{10\bar{1}0\}$ fiber component of the texture. The 'elongation' of the PF central peak is in most areas oriented parallel to the radius of the wire. The introduction of this scatter results in decreased intensity of the texture, with respect

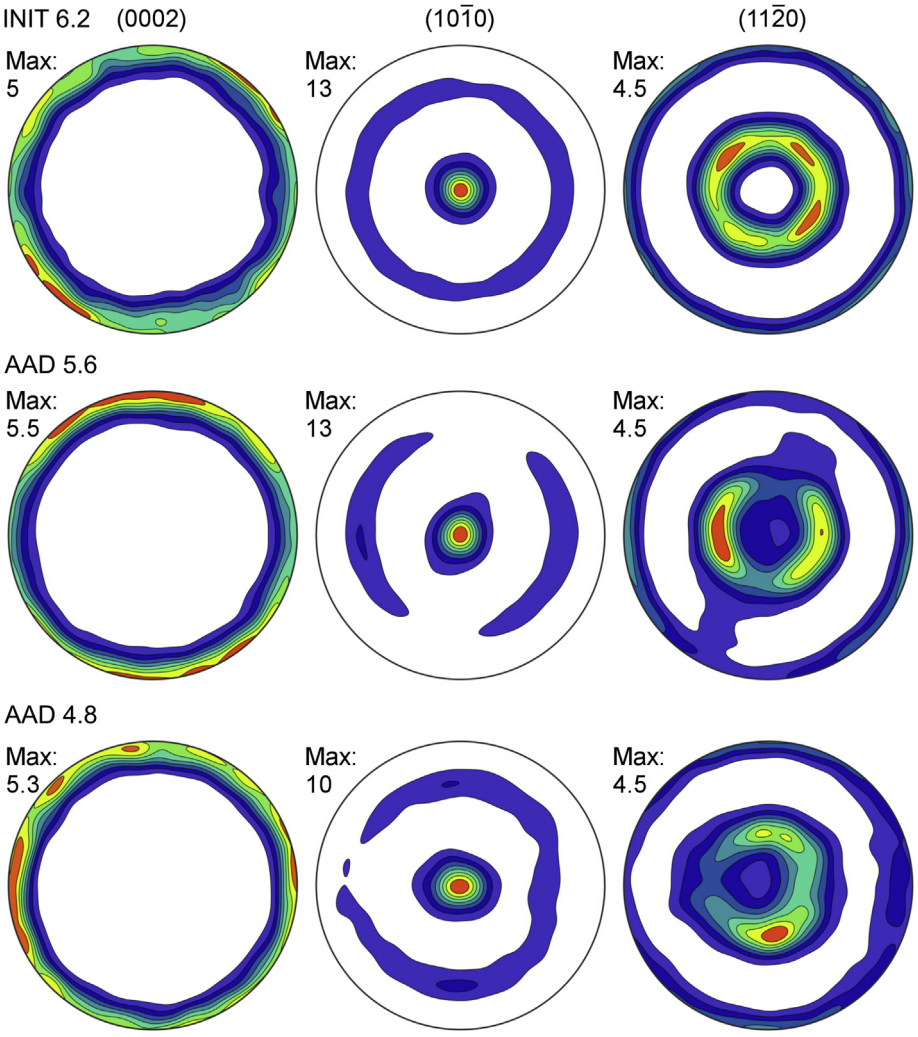

Fig. 6. Pole figures calculated from the EBSD crystal orientation data of the Ti6Al4V samples after different stages of the AAD process: INIT 6.2 (upper row); AAD 5.6 (middle row); AAD 4.8 (lower row).

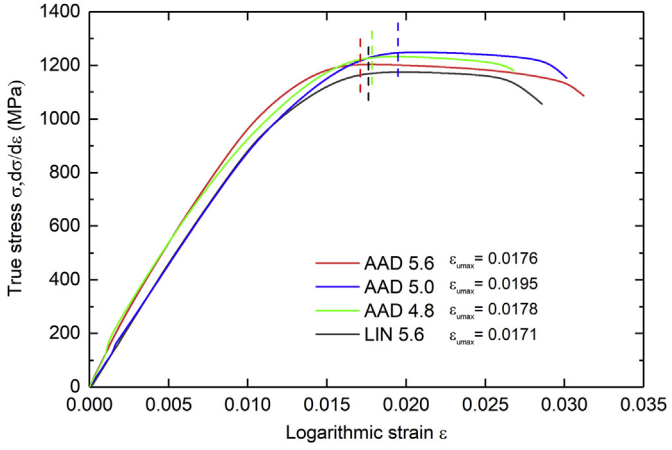

Fig. 7. Logarithmic strain-true stress curves obtained from tensile test performed on wires after subsequent stages of the AAD. Uniform elongation values marked using the Consideré criterion.

to LIN 5.6 M PF where the axial symmetry is retained. In the case of the AAD 5.6, in addition to elongation of central peak, the secondary ring in the PF is affected, and clearly there are two distinct regions with differentiated character of introduced texture asymmetry. The biggest qualitative changes in the PF are observed in the sample AAD 5.6 for areas E01, E02, E03 and E08. These areas are associated with strain softening. On the other hand, in the areas where PF is least affected (E05, E06, E07) the measured hardness values are the closest to hardness values of the initial sample INIT 6.2 (Fig. 8a). The asymmetry parameters (error values) have been calculated for all analyzed PF (Fig. 10a). The correlation with hardness distributions presented in Fig. 8a can be clearly observed. Inhomogeneity of PF asymmetry parameter is observed in the AAD 5.6 sample. On the other hand, in LIN 5.6 sample where no axially asymmetric deformation mode was applied during the drawing process, the distribution of PF asymmetry parameter is relatively homogeneous.

4. Discussion

The observed increase in the PF asymmetry is connected to deformation softening both during the AAD and LIN drawing. In the case of AAD 5.6 wire a correlation between (10$\bar{1}$0) PF asymmetry and measured hardness value is presented in Fig. 8b.

Orientation dependence of hardness presented here is corroborated by results published by Zambaldi et al. [17], where highest values of indentation depth were observed for nanoindented α-titanium grains close to [2$\bar{1}\bar{1}$0] orientation. In the present study the softening is observed in sample areas where {10$\bar{1}$0} fiber texture is partially randomized resulting in increased intensity of [2$\bar{1}\bar{1}$0] orientation component.

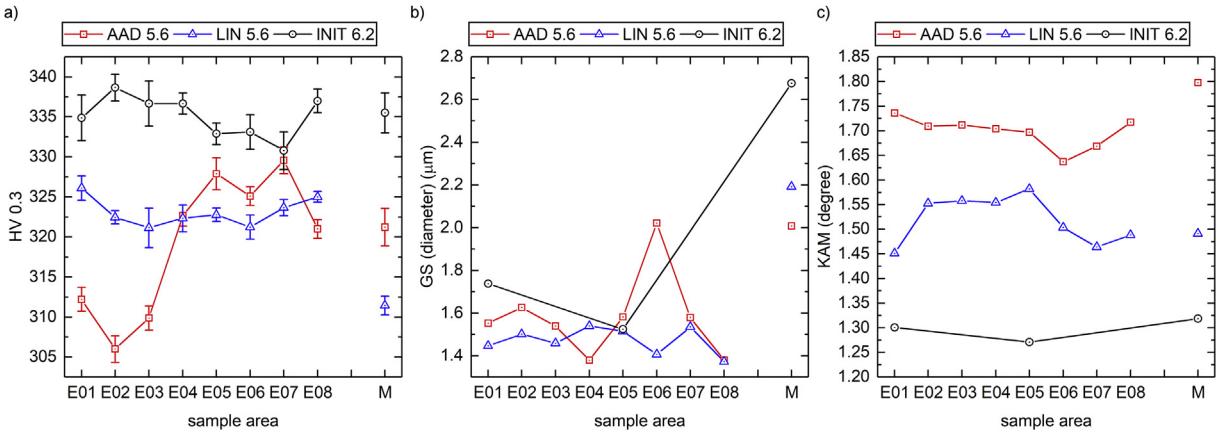

Fig. 8. Analysis of mechanical and structural inhomogeneity on the cross sections of Ti6Al4V wires: a) Vickers hardness distribution; b) grain size distribution; c) average KAM value distribution.

As mentioned before, during the drawing process the Ti6Al4V wire is repeatedly deformed by tension in the drawing direction, which involves activation of the prismatic slip. Because there is no change in the deformation mode between consecutive passes through the drawing dies, dislocation slip is activated on the same crystallographic planes leading to increase in the texture intensity and rapid work hardening of activated slip systems. This is observed in case of the LIN 5.6 M pole figure, where the asymmetry is the lowest, while the pole figure maximum intensity increases from 13 in INIT 6.2 (Fig. 6) to 15. It can be assumed that in the AAD 5.6 sample in the areas where the highest PF asymmetry is observed, additional texture components are introduced during the AAD process due to the activation of additional deformation modes. Since the stepped setup of the AAD is inherently asymmetric, those additional texture components are introduced inhomogeneously in the areas of the wire where the strain path change effect is most pronounced. The Schmid factor analysis performed for the EBSD data sets (Fig. 11) indicates that new grain orientations introduced in areas characterized by high PF asymmetry and strain softening (E01-E03 and E08) are more favorably oriented for $11\bar{2}0\ \{10\bar{1}0\}$ prismatic slip, as well as for $11\bar{2}3\ \{11\bar{2}2\}$ 2nd order pyramidal slip.

As presented in Fig. 11 a,d, additional grain orientations appeared in the AAD 5.6 sample resulting in shift towards the high values on Schmid factor distribution plots. This is especially visible in the case of $c + a$ pyramidal slip where additional high peaks appeared in the Schmid factor distribution (Fig. 11d). On the other hand, the LIN 5.6 sample has almost identical distributions of Schmid factors in all measurement areas, and the Schmid factor distributions are concentrated around lower values for the prismatic and pyramidal slip systems.

Additional analysis was performed in an attempt to identify active slip systems in the investigated Ti6Al4V alloy during the AAD processing. The TEM observation was conducted for samples extracted from the area of AAD5.6 wire corresponding to the highest asymmetry measured (E02). However due to the high density of accumulated lattice defects (Fig. 12a) the exact analysis of dislocations type and density through the HRTEM or the invisibility method [18] was not possible. Next, the XRD analysis was performed on the transverse AAD 5.6 sample, and the modified Williamson - Hall method [19] was used for the dislocation density estimation. In order to confirm the presence of dislocation types the following three combinations of slip systems were assumed: 1) basal a and prismatic a; 2) prismatic a and pyramidal $c + a\ \{10\bar{1}1\}$; 3) prismatic a, pyramidal $c + a\ \{10\bar{1}1\}$, and pyramidal $c + a\ \{11\bar{2}2\}$. The Williamson – Hall plots for each of these slip system combinations are presented in Fig. 12 b-d. Dislocation densities and calculated size of coherent domain for each combination are presented in Table 1. The R-square parameters indicate that the best fit is obtained when prismatic and both 1st and 2nd order pyramidal $c + a$ slip systems are assumed. In case of only prismatic and 1st order pyramidal $c + a$ the fit is still relatively good, but R-square is decreased, while for a prismatic and a basal the linear fit is significantly worse. The

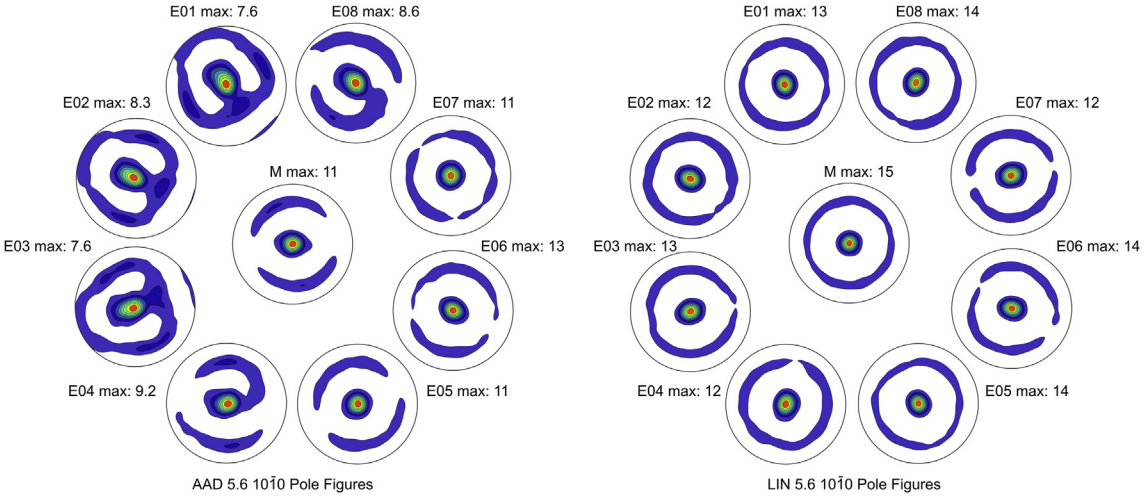

Fig. 9. Local microtexture variation on the cross-section surface of the Ti6Al4V samples after the AAD (left) and the linear/straight drawing (right). The pole figures are calculated from the EBSD maps measured in areas E01-E08 (near the edge of wire) and in area M (in the middle of the wire).

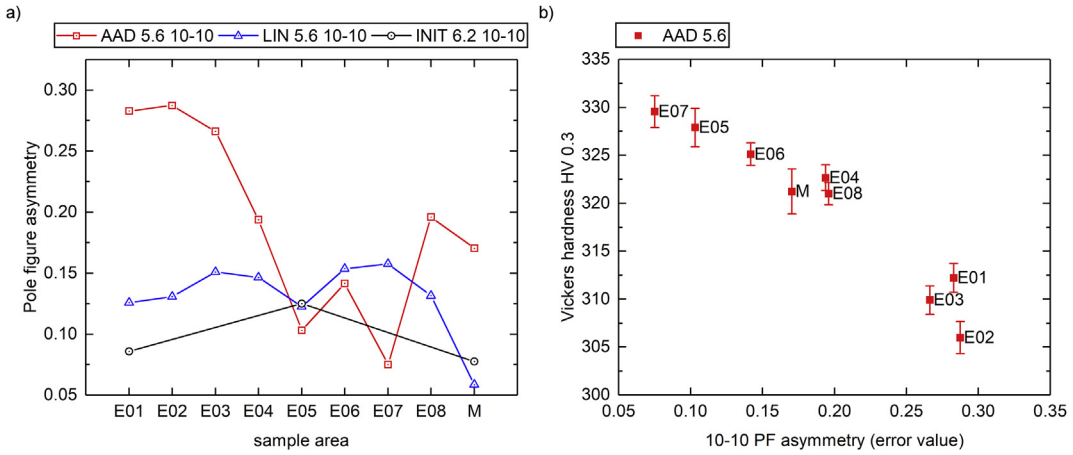

Fig. 10. a) Distribution of local pole figure asymmetry parameters for INIT 6.2, AAD 5.6 and LIN 5.6 samples; b) correlation between local mechanical properties (hardness value) and local texture asymmetry parameter in AAD 5.6 sample.

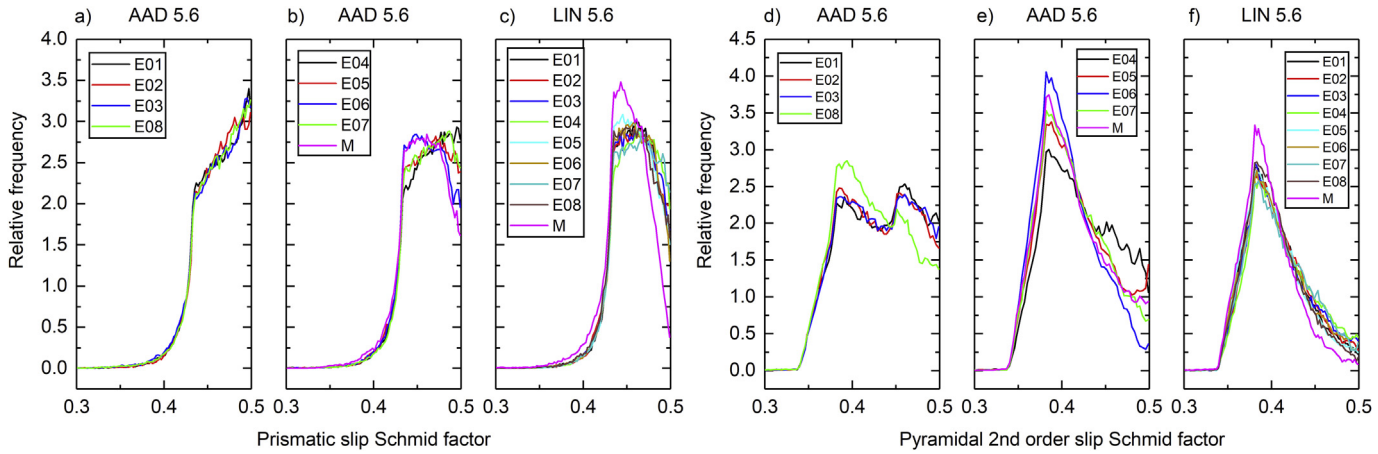

Fig. 11. Schmid factor analysis in AAD 5.6 (a,b,d,e) and LIN 5.6 (c,f) samples. For clarity the Schmid factor distributions for AAD 5.6 prismatic (a,b) and pyramidal (d,e) slip system are divided in the separate plots according to the measurement area. (For interpretation of the references to color in this figure legend, the reader is referred to the Web version of the article.). (For interpretation of the references to color in this figure legend, the reader is referred to the Web version of this article.)

dislocation density obtained with the third assumed slip system combination (Table 1) for alpha titanium is in agreement with values obtained for alpha phase in alpha-beta titanium TC6 alloy [20] deformed to similar strain as in the case of AAD 5.6 sample.

In the light of the analysis presented here, the increased plasticity due to activation of $c + a$ $\{11\bar{2}2\}$ pyramidal slip, would be tempting yet a controversial conclusion. The $c + a$ on $\{11\bar{2}2\}$ have been reported for all hcp metals except for titanium and zirconium, with the inclusion of the Ti6Al4V alloy where $c + a$ dislocations have been observed mostly on $\{10\bar{1}1\}$ planes [21–24]. Nevertheless it was suggested by computer simulations, and later shown experimentally that $c + a$ dislocations can glide on $\{11\bar{2}2\}$planes in titanium under shear stress conditions,

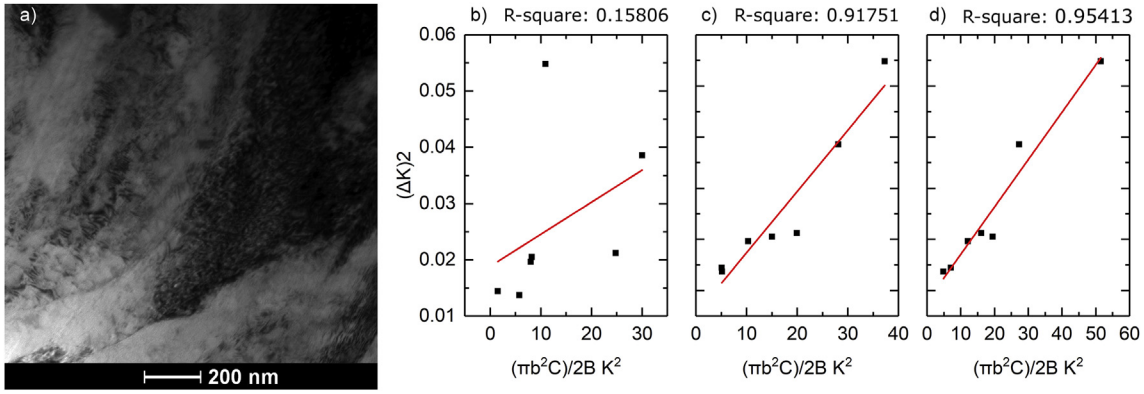

Fig. 12. a) TEM image of dislocations in titanium alpha grains (sample AAD5.6). Williamson – Hall plots for assumed slip system combinations: b) basal a and prismatic a; c) prismatic a and pyramidal $c + a\{10\bar{1}1\}$; d) prismatic a, pyramidal $c + a\{10\bar{1}1\}$, and pyramidal $c + a\{11\bar{2}2\}$, where: K - the length of the diffraction vector, b - the Burgers vector of dislocations., C – average contrast factor of dislocations in the case of a particular reflection, B – the parameter determined by the effective outer cutoff radius of dislocations.

Table 1
Size of the coherently diffracting domain (crystallite) D and dislocation density ρ calculated for assumed slip systems.

Assumed slip systems	D [nm]		ρ [1/nm^2]	
Basal $< a >$ and prismatic $< a >$	6.6	± 1.6	0.0006	± 0.0006
Prismatic $< a >$ and pyramidal $< c+a >$ $(10\bar{1}1)$	12.2	± 3.7	0.0012	± 0.0002
Prismatic $< a >$ and pyramidal $< c+a >$ $(10\bar{1}1)$ and pyramidal $< c+a >$ $(11\bar{2}2)$	10.2	± 1.5	0.0009	± 0.0001

corresponding to compression along the c axis, and specifically as accommodation slips around deformation twins [25]. While in the Ti6Al4V deformed by the AAD the twinning is not observed, conditions where grains are compressed along the *c* axis are certainly met, as those directions are parallel to the wire diameter which is being reduced. The source and operation mechanism of $c + a$ dislocations was also investigated in-situ in the transmission electron microscopy (TEM) nanocompression experiments [26], where $c + a$ dislocation growth and propagation was observed in grain with the Schmid factor for $11\bar{2}3$ $\{11\bar{2}2\}$ slip system at 0.45. On the other hand, mobility of $c + a$ dislocations in the same study was reported as low, and their pileup was connected to significant work hardening of the sample. It is, therefore, difficult to conclude whether or not the $c + a$ $\{11\bar{2}2\}$ slip is involved in the introduction of observed additional texture components. A detailed TEM study of dislocation activity in the Ti6Al4V alloy after the AAD process was beyond the scope of the current study but is considered to further investigate the reported increase in plasticity.

5. Conclusions

The AAD process was successfully applied in order to deform the Ti6Al4V wires at room temperature to $\varepsilon \sim 0.51$, which was previously impossible using the conventional linear drawing technique. The increased plasticity is attributed to application of deformation path change during the AAD, resulting in activation of additional deformation modes. The changes of the deformation path are responsible for introduction of additional texture components, and texture randomization. Resulting texture asymmetry has inhomogeneous distribution across the cross section of the wire and is connected to inhomogeneous sample softening due to application of the AAD process. The microstructure parameters such as average grain size and distribution, as well as presence of subgrain structure quantified by KAM parameter was shown to have less influence on hardness values than texture variation. The continuous dynamic recrystallization process was suggested as a possible mechanism influencing microstructure and texture evolution during the AAD. In the areas with measurable sample softening, the introduction of texture components with grain orientations more favorable for *a* prismatic and $c + a$ pyramidal slip was observed.

Data availability

The raw/processed data required to reproduce these findings cannot be shared at this time as the data also forms part of an ongoing study.

Acknowledgements

The work was performed with the financial support from the Polish National Science Centre under grant number: UMO-2015/19/B/ST8/01079. I.J.B. acknowledges financial support from the National Science Foundation (NSF CMMI-1728224).

References

[1] G. Lütjering, J.C. Williams, Titanium, Springer Berlin Heidelberg, Berlin, Heidelberg, 2007, https://doi.org/10.1007/978-3-540-73036-1.
[2] I.P. Polmear, Light Alloys - from Traditional Alloys to Nanocrystals, (2006), https://doi.org/10.1017/CBO9781107415324.004.
[3] C. Leyens, M. Peters, Titanium and Titanium Alloys, Wiley-VCH Verlag GmbH & Co. KGaA, Weinheim, FRG, 2003, https://doi.org/10.1002/3527602119.
[4] J.C. Williams, R.G. Baggerly, N.E. Paton, Deformation behavior of HCP Ti-Al alloy single crystals, Metall. Mater. Trans. A 33 (2002) 837–850, https://doi.org/10.1007/s11661-002-1016-2.
[5] Y. Wang, J. Huang, Texture analysis in hexagonal materials, Mater. Chem. Phys. 81 (2003) 11–26, https://doi.org/10.1016/S0254-0584(03)00168-8.
[6] K. Muszka, Modelling of deformation inhomogeneity in the angular accumulative drawing process-multiscale approach, Mater. Sci. Eng. A 559 (2013) 635–642, https://doi.org/10.1016/j.msea.2012.09.003.
[7] K. Muszka, L. Madej, J. Majta, The effects of deformation and microstructure inhomogeneities in the Accumulative Angular Drawing (AAD), Mater. Sci. Eng. A 574 (2013) 68–74, https://doi.org/10.1016/j.msea.2013.03.024.
[8] Y.J. Chen, Y.J. Li, J.C. Walmsley, S. Dumoulin, P.C. Skaret, H.J. Roven, Microstructure evolution of commercial pure titanium during equal channel angular pressing, Mater. Sci. Eng. A 527 (2010) 789–796, https://doi.org/10.1016/j.msea.2009.09.005.
[9] J. Kawałko, M. Wroński, M. Bieda, K. Sztwiertnia, K. Wierzbanowski, D. Wojtas, M. Łagoda, P. Ostachowski, W. Pachla, M. Kulczyk, Microstructure of titanium on complex deformation paths: comparison of ECAP, KOBO and HE techniques, Mater. Char. 141 (2018) 19–31, https://doi.org/10.1016/j.matchar.2018.04.037.
[10] J. Kawałko, P. Bobrowski, P. Koprowski, A. Jarzębska, M. Bieda, M. Łagoda, K. Sztwiertnia, Microstructure evolution of CP titanium during deformation in KoBo process followed by cold rolling, J. Alloy. Comp. 707 (2017) 298–303, https://doi.org/10.1016/j.jallcom.2016.11.202.
[11] K. Kowalczyk-Gajewska, K. Sztwiertnia, J. Kawałko, K. Wierzbanowski, M. Wronski, K. Frydrych, S. Stupkiewicz, H. Petryk, Texture evolution in titanium on complex deformation paths: experiment and modelling, Mater. Sci. Eng. A 637 (2015) 251–263, https://doi.org/10.1016/j.msea.2015.04.040.
[12] F. Bachmann, R. Hielscher, H. Schaeben, Texture analysis with MTEX – free and open source software toolbox, Solid State Phenom. 160 (2010) 63–68 10.4028/www.scientific.net/SSP.160.63.
[13] H. El Kadiri, J. Kapil, A.L. Oppedal, L.G. Hector, S.R. Agnew, M. Cherkaoui, S.C. Vogel, The effect of twin–twin interactions on the nucleation and propagation of {10-12} twinning in magnesium, Acta Mater. 61 (2013) 3549–3563, https://doi.org/10.1016/j.actamat.2013.02.030.
[14] K.S. Suresh, N.P. Gurao, S. Singh, S. Suwas, K. Chattopadhyay, S.V. Zherebtsov, G.A. Salishchev, Effect of equal channel angular pressing on grain refinement and texture evolution in a biomedical alloy Ti\13Nb\13Zr, Mater. Char. 82 (2013) 73–85, https://doi.org/10.1016/j.matchar.2013.05.003.
[15] S. Gourdet, F. Montheillet, A model of continuous dynamic recrystallization, S. Gourdet, F. Mon, Acta Mater. 51 (2003) 2685–2699, https://doi.org/10.1016/S1359-6454(03)00078-8.
[16] K. Huang, R.E. Logé, A review of dynamic recrystallization phenomena in metallic materials, Mater. Des. 111 (2016) 548–574, https://doi.org/10.1016/J.MATDES.2016.09.012.
[17] C. Zambaldi, Y. Yang, T.R. Bieler, D. Raabe, Orientation informed nanoindentation of α-titanium: indentation pileup in hexagonal metals deforming by prismatic slip, J. Mater. Res. 27 (2012) 356–367, https://doi.org/10.1557/jmr.2011.334.
[18] S. Zaefferer, A study of active deformation systems in titanium alloys: dependence on, Mater. Sci. Eng. A 344 (2003) 20–30, https://doi.org/10.1016/S0921-5093(02)00421-5.
[19] I.C. Dragomir, T. Ungár, Contrast factors of dislocations in the hexagonal crystal system, J. Appl. Crystallogr. 35 (2002) 556–564, https://doi.org/10.1107/S0021889802009536.
[20] R. Shi, Z. Nie, Q. Fan, F. Wang, Y. Zhou, X. Liu, Correlation between dislocation-density-based strain hardening and microstructural evolution in dual phase TC6 titanium alloy, Mater. Sci. Eng. A 715 (2018) 101–107, https://doi.org/10.1016/j.msea.2017.12.098.
[21] I.P. Jones, W.B. Hutchinson, Stress-state dependence of slip in Titanium-6Al-4V and other H.C.P. metals, Acta Metall. 29 (1981) 951–968, https://doi.org/10.1016/0001-6160(81)90049-3.
[22] R. Ding, J. Gong, A.J. Wilkinson, I.P. Jones, $< c + a >$ Dislocations in deformed Ti-6Al-4V micro-cantilevers, Acta Mater. 76 (2014) 127–134, https://doi.org/10.1016/j.actamat.2014.05.010.
[23] M.H. Yoo, J.R. Morris, K.M. Ho, S.R. Agnew, Nonbasal deformation modes of HCP metals and alloys: role of dislocation source and mobility, Metall. Mater. Trans. A 33 (2002) 813–822, https://doi.org/10.1007/s11661-002-1013-5.
[24] C. Lavogiez, S. Hémery, P. Villechaise, Concurrent operation of $< c + a >$ slip and twinning under cyclic loading of Ti-6Al-4V, Scr. Mater. 157 (2018) 30–33, https://doi.org/10.1016/j.scriptamat.2018.07.033.
[25] Y. Minonishi, S. Morozumi, H. Yoshinaga, {1122} < 1123 > slip in titanium, Scr. Metall. 16 (1982) 427–430, https://doi.org/10.1016/0036-9748(82)90166-1.
[26] Q. Yu, J. Sun, J.W. Morris, A.M. Minor, Source mechanism of non-basal h c + a i slip in Ti alloy, Scr. Mater. 69 (2013) 57–60, https://doi.org/10.1016/j.scriptamat.2013.03.009.